

Pre-Supernova Eruptions Triggered by Sudden Energy Deposition in Low-Mass Core-Collapse Supernova Progenitors

SHUAI ZHA ,¹ HAN LIN,¹ XUEFEI CHEN ,¹ AND ZHANWEN HAN ¹

¹*International Centre of Supernovae (ICESUN), Yunnan Key Laboratory of Supernova Research, Yunnan Observatories, Chinese Academy of Sciences (CAS), Kunming 650216, People's Republic of China*

ABSTRACT

In low-mass core-collapse supernova (CCSN) progenitors, nuclear burning beyond oxygen can become explosive under degenerate conditions, triggering eruptive mass loss before the final explosion. We investigate such pre-SN eruptions using SNEC hydrodynamic simulations and realistic stellar models, parameterizing the nuclear energy deposition as a fraction of the binding energy of the combined He layer and H-rich envelope. For the lowest-mass model ($9 M_{\odot}$), the ejecta mass (M_{ej}) scales with the energy gained by the H-rich envelope via a power law (index ~ 3.5). Across $9\text{--}10 M_{\odot}$, this relation shows limited scatter within a factor of ~ 2.6 , enabling an estimation of the gained energy from M_{ej} . The shock passage also flattens the bound envelope, which can affect the SN light curve morphology and provide another diagnostic for the eruption. Then, we compute the associated precursor light curves for the $9 M_{\odot}$ model with the multi-group radiative-transfer code **STELLA**. These signals are typically faint, with bolometric luminosities of $\sim 10^{39} \text{ erg s}^{-1}$ lasting hundreds of days. Their cool black-body spectra make them brighter in the infrared, yet several magnitudes fainter than observed pre-SN precursors at the threshold for full envelope ejection. To aid future studies, we make our post-eruption stellar profiles and precursor light curves publicly available.

Keywords: Core-collapse supernovae (304) — Late stellar evolution (911) — Circumstellar matter (241) — Transient sources (1851)

1. INTRODUCTION

Core-collapse supernovae (CCSNe), the explosive deaths of massive stars with a zero-age main-sequence mass (M_{ZAMS}) greater than $\sim 8\text{--}10 M_{\odot}$ (e.g. S. J. Smartt 2009; D. Ibeling & A. Heger 2013), constitute a major class of research objects for wide-field time-domain astronomical surveys (see e.g., M. J. Graham et al. 2019; Ž. Ivezić et al. 2019; B. Shappee et al.

2014; J. L. Tonry et al. 2018; K. C. Chambers et al. 2016; T. Wang et al. 2023; X. Yuan et al. 2020). Thanks to the high cadence of modern surveys and their rapid follow-up observations, a growing sample of hydrogen-rich CCSNe, i.e. Type II supernovae (SNe II), observed at early phases exhibits the features of interactions with dense circumstellar material (CSM) surrounding their progenitor stars (D. C. Leonard et al. 2000; A. Gal-Yam et al. 2014; N. Smith et al. 2015; D. Khazov et al. 2016; O. Yaron et al.

2017; F. Förster et al. 2018; R. J. Bruch et al. 2021, 2023). This CSM directly manifests the mass-loss activities during the final evolutionary stages (the last months to years) of CCSN progenitors (N. Smith 2017), thereby serving as a powerful diagnostic for probing the final phases of massive stars immediately preceding their explosion.

Stars undergo mass loss throughout their lifetimes, and for single stars, stellar evolutionary models typically incorporate empirical prescriptions for steady-state, radiation- or dust-driven winds (R. Kippenhahn et al. 2013; N. Langer 2012). However, R. J. Bruch et al. (2021, 2023) inferred that >30% of SN II progenitors—likely red supergiants (RSGs)—experienced enhanced mass loss immediately before explosion to form dense and confined CSM, with rates exceeding standard prescriptions. Several models have been proposed to resolve the tension without invoking significantly elevated mass loss rates, such as accelerating winds (P. D. Bennett 2010; T. J. Moriya et al. 2017), a pre-explosion effervescent zone (N. Soker 2021), or a dense chromosphere (L. Dessart et al. 2017; J. Fuller & D. Tsuna 2024). Another intriguing way to form the observed dense CSM is a brief episode of eruptive mass loss (L. Dessart et al. 2010; E. Quataert & J. Shiode 2012; N. Smith & W. D. Arnett 2014; V. Morozova et al. 2020; N. Kuriyama & T. Shigeyama 2020; S.-C. Leung & J. Fuller 2020; C. D. Matzner & S. Ro 2021; T. Matsumoto & B. D. Metzger 2022; D. Tsuna et al. 2023; S. J. Cheng et al. 2024). The eruptive scenario finds observational support in the appearance of nearby SN IIP progenitors (B. Davies & E. R. Beasor 2020; B. Davies et al. 2022). More direct evidence for such eruptions comes from outbursts preceding interacting SNe (J. Maza et al. 2009; R. J. Foley et al. 2011; J. C. Mauerhan et al. 2013; E. O. Ofek et al. 2014; C. Bilinski et al. 2015; S. J. Brennan et al. 2024; A. Pastorello et al. 2025), with 18 cases observed

prior to Type IIn SNe by the Zwicky Transient Facility (ZTF) in 2018-2020 (N. L. Strotjohann et al. 2021). However, with the notable exception of SN 2020tlf—the first normal Type IIP/L supernova with confirmed precursor emission (W. V. Jacobson-Galán et al. 2022)—such activity appears to be typically too faint to observe in other normal SNe II.

The physical mechanism(s) responsible for such late-stage, pre-SN eruptions remain elusive, with candidates including internal gravity waves (E. Quataert & J. Shiode 2012; J. Fuller 2017), instabilities of advanced nuclear burning (W. D. Arnett & C. Meakin 2011; N. Smith & W. D. Arnett 2014), opacity-driven super-Eddington luminosities (Y.-F. Jiang et al. 2018; S. J. Cheng et al. 2024), electron-positron pair instabilities (Z. Barkat et al. 1967; S. E. Woosley et al. 2007), and binary interactions (R. A. Chevalier 2012; B. Danieli & N. Soker 2019). Several numerical surveys have studied the eruptive scenario for CCSN progenitors with initial masses above $11 M_{\odot}$, exploring both sudden and continuous energy deposition at various locations within the star (see e.g., L. Dessart et al. 2010; V. Morozova et al. 2020; D. Tsuna et al. 2023). S. P. Owocki et al. (2019) has explored such eruptions in very massive stars ($100 M_{\odot}$) in the context of Luminous Blue Variable stars. To complement these efforts, we conduct a systematic study of low-mass CCSN progenitors with M_{ZAMS} between 9 and $10 M_{\odot}$. Despite the narrow mass range, such stars are relatively abundant, constituting $\sim 22\%$ of all SN II progenitors under the assumption of a bottom-heavy, power-law initial mass function (slope $\alpha = -2.35$, E. E. Salpeter 1955) and an upper mass limit of $18 M_{\odot}$ (S. J. Smartt 2015). They are the leading progenitor channel for low-luminosity SNe II (J. R. Maund et al. 2005; S. D. Van Dyk et al. 2012; K. K. Das et al. 2025a,b; H. Lin et al. 2025).

Theoretical stellar evolution models are scarcer for low-mass CCSN progenitors than for their more massive counterparts, largely due to the numerical challenges of simulating off-center nuclear flashes and flames in partially degenerate cores during advanced burning stages (beyond carbon burning; S. E. Woosley et al. 1980; K. Nomoto & M.-A. Hashimoto 1986; S. Jones et al. 2013, 2014; S. E. Woosley & A. Heger 2015; M. Limongi et al. 2024). In particular, explosive off-center nuclear flashes in advanced burning shells (e.g. silicon) provide a unique physical mechanism that releases energy in a short period and triggers pre-SN eruptions of progenitor stars with $M_{\text{ZAMS}} \sim 9\text{-}10 M_{\odot}$, potentially giving rise to faint IIP-like precursor transients (T. A. Weaver & S. E. Woosley 1979; S. E. Woosley & A. Heger 2015). The timing, location, and intensity of this violent energy release—and its subsequent deposition in the outer mantle—are highly uncertain, as they depend on the detailed ignition conditions of the nuclear flashes. Here, we conduct a parameter study of this eruptive phenomenon to quantify the relationship between the amount of energy deposition and the resulting mass ejection and precursor signals.

Our paper is organized as follows. Section 2 details our investigation of the eruptive mass loss through non-radiative hydrodynamics simulations with parameterized energy deposition. We detail our simulation methodology and progenitor models (§ 2.1), present a detailed analysis of the $9.0 M_{\odot}$ case (§ 2.2), and explore the progenitor dependence (§ 2.3). Section 3 presents the associated precursor signals generated with the multi-group radiative-hydrodynamics code **STELLA**. We discuss the caveats of our study in Section 4 and conclude our findings in Section 5.

2. ERUPTION SIMULATION

2.1. *Simulation method and progenitors*

In our pre-SN eruption scenario, the sudden energy deposition in deep layers due to explosive nuclear flashes launches a shock wave that propagates outward, unbinding part of the stellar envelope. We model the shock propagation and the subsequent mass ejection in spherical symmetry using the Lagrangian hydrodynamics code **SNEC** (V. Morozova et al. 2015). To efficiently track the mass outflow over a sufficiently long timescale (up to 10 years), we operate **SNEC** in its non-radiative mode. The code works with the Paczynski equation of state (EOS; B. Paczynski 1983) for a mixture of ions, electrons, and photons, which is further complemented with the partial ionization of H and He through a Saha solver (M. R. Zaghoul et al. 2000; F. X. Timmes & D. Arnett 1999; F. X. Timmes & F. D. Swesty 2000).

In most of our simulations, we start by removing the progenitor’s C-O core and depositing an energy E_{dep} at the base of the He layer. In the scenario of advanced nuclear flashes, energy deposition is expected to originate from a deeper region within the core. However, due to significant uncertainty in its exact location, we adopt the base of the He layer as a uniform treatment across our models. This energy is spread over $0.1 M_{\odot}$ within 10^3 s, which is much shorter than the dynamical timescale of the envelope ($\mathcal{O}(10^6)$ s). The computational domain is discretized using a non-uniform grid consisting of 2000 zones across both the He layer and H-rich envelope. The mass resolution, defined as $\text{dq} = \text{d}M/M_{\text{tot}}$, is 2×10^{-3} at the midpoint (zone 1000), and it decreases proportionally to 2×10^{-4} at the innermost zone and 2×10^{-6} at the outermost zone. We have confirmed that using a grid with $2.5 \times$ finer resolution results in nearly identical ejected masses across the explored range of E_{dep} , compared to simulations conducted with our standard resolution.

Table 1. Properties of the stellar models

M_{ZAMS} (M_{\odot})	M_{prog} (M_{\odot})	R_{prog} (R_{\odot})	M_{He} (M_{\odot})	M_{Henv} (M_{\odot})	$E_{\text{bind,tot}}$ (10^{48} erg)	$E_{\text{bind,H}}$ (10^{47} erg)
9.0	8.75	412	0.17	7.18	2.17	0.98
9.25	8.98	404	0.33	7.20	4.92	1.31
9.5	9.21	412	0.54	7.17	7.43	1.52
9.75	9.45	445	0.75	7.14	9.37	1.46
10.0	9.68	513	0.87	7.20	9.37	0.77
10.5	10.20	542	0.98	7.52	12.44	1.12
11.0	10.70	569	1.03	7.87	16.74	1.12
12.0	10.91	635	1.04	7.78	27.21	0.88

NOTE— M_{ZAMS} is the zero-age main-sequence mass. Other quantities are at the terminal of their standard evolution: M_{prog} and R_{prog} are the stellar mass and radius; M_{He} and M_{Henv} are the masses of He layer and H-rich envelope; $E_{\text{bind,tot}}$ and $E_{\text{bind,H}}$ are the binding energy for the combined He layer and H-rich envelope, and for the H-rich envelope only, respectively. In this paper, we performed eruption simulations using 5 models with $M_{\text{ZAMS}} = 9\text{--}10 M_{\odot}$.

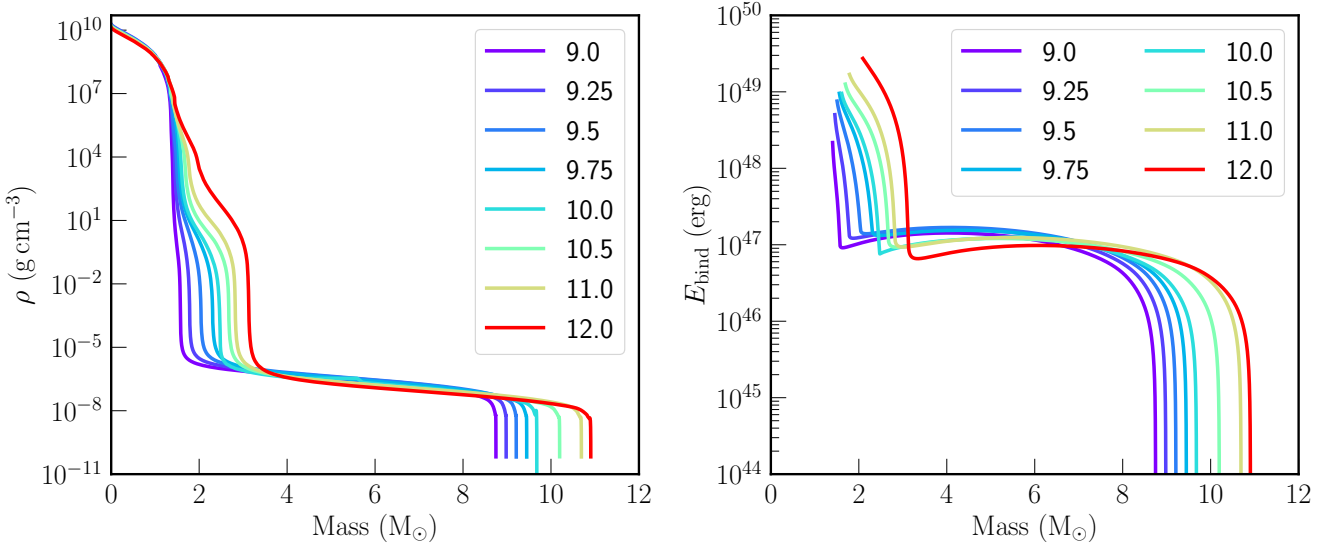


Figure 1. Profiles of density (left panel) and binding energy (right panel, computed as Eq. 1) as a function of mass coordinate for our employed progenitor models ($M_{\text{ZAMS}} = 9\text{--}10 M_{\odot}$) alongside three more massive ones up to $12 M_{\odot}$ for comparison. All models are from [T. Sukhbold et al. \(2016\)](#).

We use 5 solar-metallicity CCSN progenitor models with $M_{\text{ZAMS}} = 9\text{--}10 M_{\odot}$ in increments of $0.25 M_{\odot}$ evolved in the `Kepler` code (see Ta-

ble 1; [T. Sukhbold et al. 2016](#))² as our initial conditions. These non-rotating and single-

² This set of progenitor models was computed using erroneous pair neutrino loss rates. This mainly affects the core structure of models with $M_{\text{ZAMS}} \geq 20 M_{\odot}$.

star models are widely employed in CCSN simulations (e.g., S. M. Couch et al. 2020; G. Stockinger et al. 2020; T. Wang & A. Burrows 2024) and light-curve modeling of SNe II (B. L. Barker et al. 2022; A. Kozyreva et al. 2022; S. Zha et al. 2023; T. J. Moriya et al. 2023; M. Sato et al. 2024). The models were evolved until the immediate onset of core collapse, defined as the time when the maximum infall velocity exceeds 900 km s^{-1} in the iron core. Beyond core O burning, an RSG’s envelope is effectively “frozen” in the standard single-star evolution (S. E. Woosley et al. 2002; N. Langer 2012). Therefore, we adopt the pre-collapse envelope structure as a valid approximation for our purpose, following previous works (L. Dessart et al. 2010; D. Tsuna et al. 2023).

Table 1 summarizes the global properties of these stellar models, alongside 3 more massive cases up to $M_{\text{ZAMS}} = 12 M_{\odot}$. The $M_{\text{ZAMS}} = 9\text{-}10 M_{\odot}$ models lose 0.25-0.30 M_{\odot} in total through winds and retain H-rich envelopes of $\sim 7.2 M_{\odot}$. We list the binding energy, computed as

$$E_{\text{bind}}(M_r) = \int_{M_r}^{M_{\text{max}}} (GM'_r/r - \epsilon) dM'_r, \quad (1)$$

for the combined He layer and the H-rich envelope ($E_{\text{bind,tot}}$), and for the H-rich envelope alone ($E_{\text{bind,H}}$). Here, ϵ is the specific internal energy taken from **SNEC**. The CO/He and He/H interfaces are defined where the He and H fractions drop below 0.5, respectively. $E_{\text{bind,H}}$ is of order 10^{47} erg for all $9\text{-}12 M_{\odot}$ models, while $E_{\text{bind,tot}}$ for the $9 M_{\odot}$ model is an order of magnitude smaller than that for the $12 M_{\odot}$ model and it differs by a factor of ~ 4 within $M_{\text{ZAMS}} = 9\text{-}10 M_{\odot}$. We note that there is a $\sim 5\%$ difference in the resulting E_{bind} of **SNEC** compared to original values of **Kepler**, due to the difference in their employed equation of state. We

and has negligible impact on the envelope structure for low-mass models (T. Sukhbold et al. 2018).

use the **SNEC** values as the reference energy to ensure consistency with the hydrodynamics simulations. In addition, the given progenitor models feature layer interfaces that span a mass range of a few $10^{-3} M_{\odot}$. This smearing introduces uncertainties of several percent in $E_{\text{bind,H}}$ and $\sim 10\%$ in $E_{\text{bind,tot}}$. Therefore, any correlation established using the absolute value of E_{dep} is sensitive to these model variations, while this dependence is greatly mitigated by using fractional energy deposition ($E_{\text{dep}}/E_{\text{bind}}$) as the control parameter.

Figure 1 further shows the density and binding energy profiles as a function of the mass coordinate for these models. The **Kepler** progenitor models exhibit negative specific binding energy at the bottom of the H-rich envelope, indicating that this region is more easily ejected. This leads to a distinctive mass ejection behavior for energy deposition near the threshold of full envelope ejection. We have checked that **MESA** CCSN progenitor models (e.g., evolved with `example_ccsn_IIp` in the test suite of **MESA** revision 12778, B. Paxton et al. 2018; D. Tsuna et al. 2023), do not display this feature. This difference between stellar evolution codes merits further investigation. Finally, uncertainties in the treatment of stellar outer boundary condition (T. Sukhbold et al. 2018) and envelope convection (e.g., the mixing-length parameter and convective overshooting, A. Maeder & G. Meynet 1987; L. Dessart et al. 2013) can substantially alter the envelope structure. A comprehensive assessment of these effects is beyond the scope of this work.

In this work, we mainly discuss results with E_{dep} in the range of $0.5\text{-}1.0 \times E_{\text{bind,tot}}$. As we will demonstrate, the lower limit of 0.5 corresponds to a non-negligible fraction of mass ejection ($\sim 10^{-4}$), whereas the upper limit corresponds to the full envelope ejection. This energy deposition can be related to an explosive nuclear flash of O or Si burning, which re-

leases energy in a dynamical timescale during the late-stage evolution of low-mass CCSN progenitors (S. E. Woosley & A. Heger 2015). For instance, converting $0.01 M_{\odot}$ of O to Si releases 9.06×10^{48} erg, and converting $0.01 M_{\odot}$ of Si to Ni releases 3.74×10^{48} erg. These energy yields are on the same order as $E_{\text{bind,tot}}$, making our chosen E_{dep} physically motivated.

2.2. The $9.0 M_{\odot}$ model

2.2.1. Structural response

We first present a detailed analysis of the eruption simulations for the lowest-mass model in our set, i.e. $9.0 M_{\odot}$. This model has the smallest values for the He-layer mass and $E_{\text{bind,tot}}$. Figure 2 shows density profiles at selected times for 3 different fractional energy depositions, $f_{\text{dep}} \equiv E_{\text{dep}}/E_{\text{bind,tot}} = 0.6, 0.8$ and 1.0 . For these cases, the shock generated by the sudden energy deposition breaks out of the stellar surface at $\sim 43, 33$ and 25 days, respectively, with a shorter breakout time as f_{dep} increases. For sub- $E_{\text{bind,tot}}$ energy deposition ($f_{\text{dep}} < 1$), the He layer remains nearly static after the shock passes through it. This leads to prohibitively small timesteps ($\mathcal{O}(s)$) in the simulation due to the high sound speed in the He layer. To mitigate this, we further remove the He layer at 80 days post deposition, after which the shock has broken out of the stellar surface for all simulated cases with $f_{\text{dep}} \geq 0.5$, and continue the simulation with only the H-rich envelope. We refer to these as “H-only” simulations in contrast to the “full” simulations that include both the He layer and the H-rich envelope, which were run for at least 1 year. As shown in each panel of Figure 2, the solid gray and dashed cyan curves represent the density profiles of the full and H-only simulations 1 year after energy deposition, which are nearly identical for the overlapping regions.

Compared to the initial profile, the inner region of the evolved envelope (approximately

within R_{prog}) becomes progressively thinner and flatter as f_{dep} increases. This structural change has been suggested by R. Ouchi & K. Maeda (2019) and it will have a direct impact on the light curve of SNe II, such as making it more luminous and bluer (L. Dessart et al. 2013; S. Zha et al. 2023). R. Ouchi & K. Maeda (2021) proposed that this expansion of the H-rich envelope can explain the enhanced luminosity of some bright SNe IIP, e.g. SN 2009 kf. In the $f_{\text{dep}} = 0.6$ case, the envelope separates into two distinct parts slightly above the original stellar radius R_{prog} (the sharp density drop in the black curve). The inner region remains almost static after 1 year, while the outer region up to $\sim 10^{15}$ cm develops discontinuous features that likely lead to hydrodynamic instabilities and inhomogeneities in the CSM (B. T.-H. Tsang et al. 2022). For $f_{\text{dep}} = 0.8$, the inner region contracts slightly before stabilizing after 3 years. This static part extends to $\sim 10^{14}$ cm (or $\sim 3.5 \times R_{\text{prog}}$), with a density slope of ~ 4.9 outside $\sim R_{\text{prog}}$, while the outer part expands homologously ($v_r \propto r$). In stark contrast, the $f_{\text{dep}} = 1.0$ case results in the complete, homologous ejection of the entire H-rich envelope. If the final CCSN explosion occurs after a significant delay, it may not display the usual H recombination signature of SNe II.

2.2.2. Mass ejection process

A key question concerns how the total mass ejected and the kinematics of the ejection process depend on f_{dep} . To investigate this, we plot the ejecta mass (M_{ej}) and its mean velocity ($\langle v_{\text{ej}} \rangle$) as a function of time for $0.6 \leq f_{\text{dep}} \leq 1.0$ in Figure 3. Here, we adopt a conservative criterion for the ejecta that requires the outflow velocity to exceed the local escape velocity, $v_{\text{esc}} = \sqrt{2GM_r/r}$. A comparison of the full (solid curves) and H-only (“x” symbols) simulations shows close agreement for the overlapping periods in both panels, further demon-

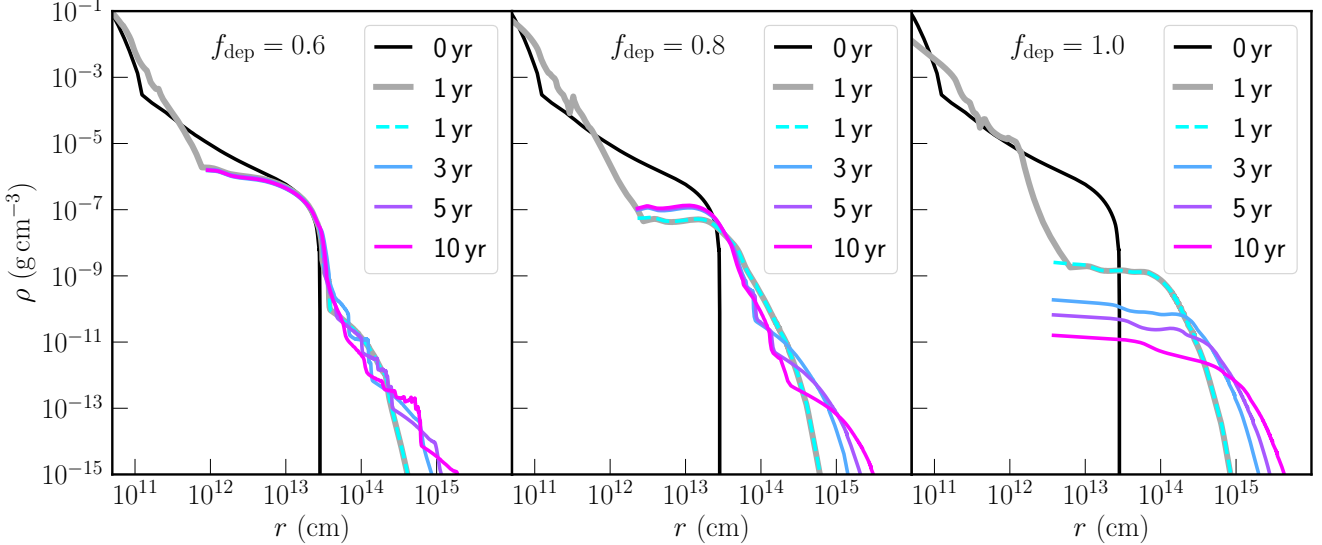


Figure 2. Density profiles as a function of radius at selected times for 3 eruption simulations using the $9 M_{\odot}$ model. Fractional energy deposition ($f_{\text{dep}} \equiv E_{\text{dep}}/E_{\text{bind,tot}}$) is 0.6, 0.8, and 1.0 from left to right. The solid gray and dashed cyan lines represent the results at 1 year for the full and H-only simulations, respectively. After 1 year, we only plot the results for the long-term H-only simulations.

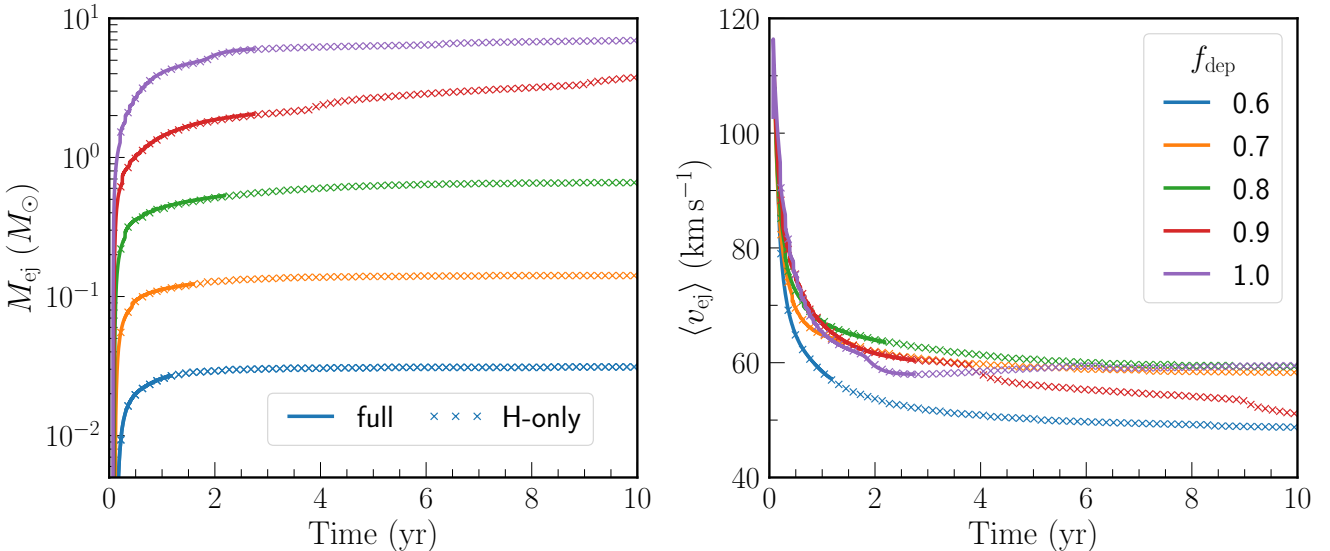


Figure 3. Time evolution of the ejecta mass (M_{ej} , left panel) and mean velocity ($\langle v_{\text{ej}} \rangle$, right panel) for selected fractional energy deposition ($f_{\text{dep}} = E_{\text{dep}}/E_{\text{bind,tot}}$). Solid curves represent the full simulations including the He layer and H-rich envelope, while “ \times ” symbols show simulations where the He layer was removed at 80 days.

ing that removing the quasi-static He layer is a valid approach. The results reveal clear trends in mass ejection kinematics. M_{ej} reaches its saturation after ~ 3 years for all values of f_{dep} except 0.9. The saturated M_{ej} increases with f_{dep} as expected. Concurrently, $\langle v_{\text{ej}} \rangle$ decreases from

an initial maximum of $\sim 120 \text{ km s}^{-1}$, $\sim 30\%$ above the original RSG’s surface escape velocity ($\sim 90 \text{ km s}^{-1}$), to a final static value of $\sim 50 \text{ km s}^{-1}$ for $f_{\text{dep}} = 0.6$ and $\sim 60 \text{ km s}^{-1}$ for all other f_{dep} values except 0.9.

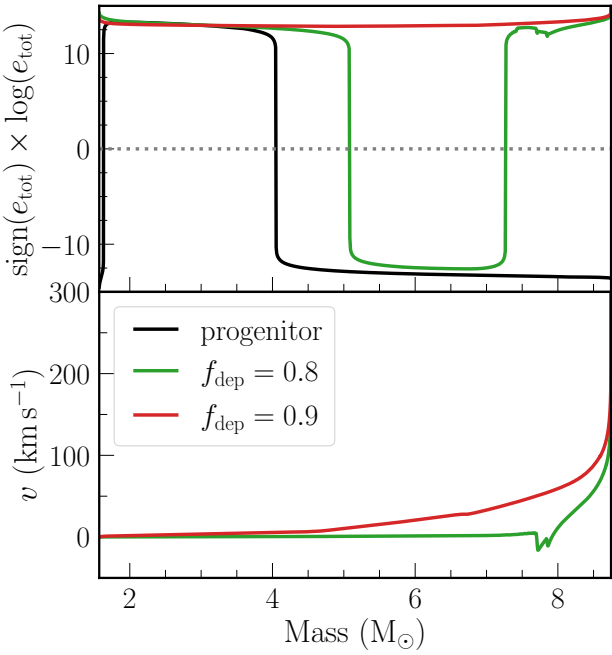


Figure 4. Profiles of total specific energy (e_{tot} ; top) and velocity (bottom) as a function of mass coordinate for the progenitor model (black) and for $f_{\text{dep}} = 0.8$ (green) and 0.9 (red) at 5 years post energy deposition. A signed logarithmic scale is used for e_{tot} to enhance clarity.

For $f_{\text{dep}} = 0.9$, both M_{ej} and $\langle v_{\text{ej}} \rangle$ exhibit correlated long-term trends, with the mass increasing and the mean velocity decreasing steadily. Superimposed on this trend are concurrent features: M_{ej} shows small jumps at ~ 4 and 9 years, while $\langle v_{\text{ej}} \rangle$ exhibits clear decreases at the same times. To diagnose this distinct behavior, we compare the total specific energy (e_{tot} , sum of gravitational, internal, and kinetic) and velocity profiles for models with $f_{\text{dep}}=0.8$ and 0.9 at 5 years post energy deposition in Figure 4. For clarity, we plot the signed logarithm of e_{tot} . As already noted in § 2.1, the progenitor model has a region of positive e_{tot} at the base of the H-rich envelope (the black curve in Figure 4). For the $f_{\text{dep}}=0.8$ case, a zone of negative e_{tot} and therefore a strictly bound region persists between the ejecta and the inner part of the envelope with positive e_{tot} . In contrast, for $f_{\text{dep}}=0.9$, the entire envelope gains positive e_{tot} , facilitating

more mass ejection but with the inner ejecta expanding at lower velocities. For MESA-like progenitors where e_{tot} is negative throughout the H-rich envelope (e.g., D. Tsuna et al. 2023), we anticipate more self-similar kinematics across the parameter space of f_{dep} with sub- $E_{\text{bind,tot}}$ deposition. Nevertheless, such a distinct behavior associated with the e_{tot} profile warrants further investigation in the modeling of CCSN progenitors.

2.2.3. $M_{\text{ej}}-f_{\text{dep}}$ relation

Lastly, we quantify the relationship between M_{ej} and f_{dep} for the $9.0 M_{\odot}$ model using a suite of simulations with f_{dep} ranging from 0.5 and 1.0 in increments of 0.025 . In the left panel of Figure 5, black bars show M_{ej} at 1 , 5 and 10 years post energy deposition from bottom to top, and open circles mark the data at 3 years. We find three distinct regions for mass ejection: for $f_{\text{dep}} \lesssim 0.85$, M_{ej} saturates within 3 years; for $f_{\text{dep}} \gtrsim 1.0$, the entire H-rich envelope is ejected within 3 years. A portion of the He layer can also be stripped for $f_{\text{dep}} \gtrsim 1.0$. In the intermediate regime ($0.85 \lesssim f_{\text{dep}} \lesssim 1.0$), M_{ej} increases over the long term, with nearly the entire H-rich envelope ejected by 10 years for $f_{\text{dep}} \gtrsim 0.95$. A power-law fit to the 3 -year data (open circles) yields $M_{\text{ej}} \propto f_{\text{dep}}^{10.6}$, indicating a very sensitive dependence. N. Kuriyama & T. Shigeyama (2020) have reported a similarly quick increase in M_{ej} with f_{dep} for more massive RSGs and yellow supergiants.

Recognizing that only the energy gained by the H-rich envelope (E_{gain}) drives the final eruptive mass loss, we further examine the dependence of mass ejection on E_{gain} . The right panel of Figure 5 shows M_{ej} as a function of the fractional energy gain, $f_{\text{gain}} = E_{\text{gain}}/E_{\text{bind,H}}$. The entire H-rich envelope is ejected for $f_{\text{gain}} \gtrsim 4$. The relation is well-described by a power law with an index of ~ 3.5 (dashed magenta curve), which is consistent with values found in sim-

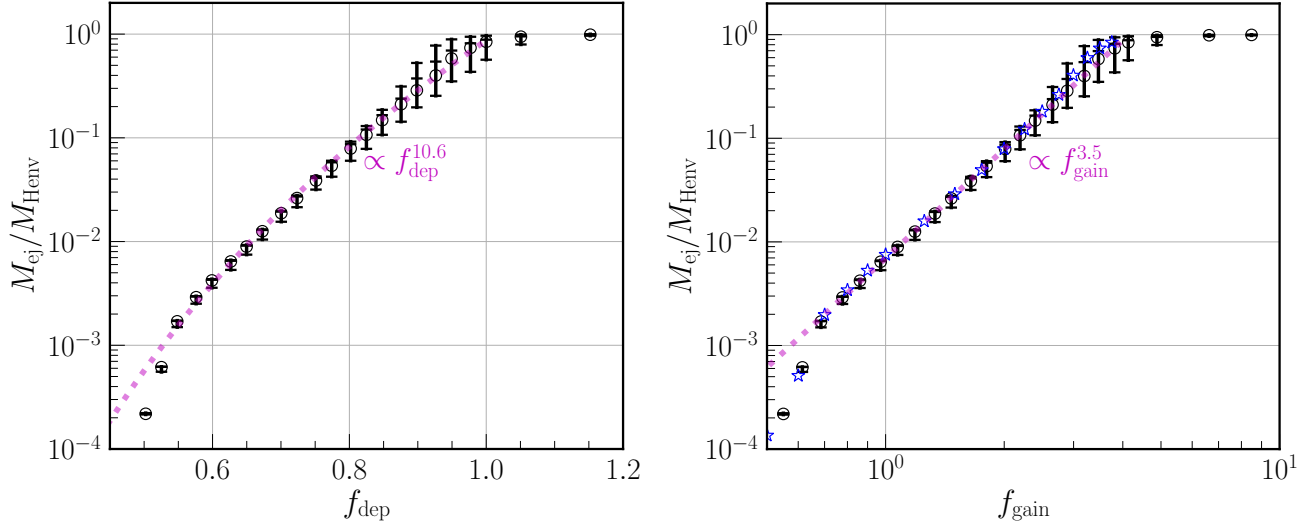


Figure 5. The fraction of ejected mass relative to the mass of the H-rich envelope ($M_{\text{ej}}/M_{\text{Henv}}$) as a function of fractional energy deposition (f_{dep} , left panel) and fractional energy gained by the H-rich envelope (f_{gain} , right panel). Black bars show the results at 1, 5 and 10 years (from bottom to top) while the open circles mark the results at 3 years after energy deposition. In each panel, the magenta curves is a power-law fit to the data. In the right panel, the blue stars show the results with fractional energy deposited at the base of the H-rich envelope which show excellent agreement with the main results.

ulations with polytropic stars (I. Linial et al. 2021; N. J. Corso & D. Lai 2024). Specifically, I. Linial et al. (2021) obtained indices of 1.79–4.17 for a polytropic index n of 1.5, closely resembling our RSG envelope. We further validate this relation using a separate simulation set where energy is deposited directly at the base of the H-rich envelope (blue open stars). In this configuration, f_{gain} is equivalent to f_{dep} . The excellent agreement confirms that the mass eruption is primarily controlled by E_{gain} . Therefore, since a significant portion of the energy at deeper layers is consumed before reaching the envelope, the ejecta mass directly reflects E_{gain} rather than the total E_{dep} . Inferring the true energy deposition and its underlying physical mechanism requires a comprehensive analysis that incorporates energy release into realistic stellar evolutionary models.

2.3. Progenitor dependence

We explore the progenitor dependence within $M_{\text{ZAMS}} = 9\text{--}10 M_{\odot}$, scanning f_{dep} from 0.5 to 1.0 in increments of 0.05. Figure 6 shows the re-

sulting ejected mass (M_{ej} , evaluated at 3 years post energy deposition) as a function of M_{ZAMS} and energy deposition. The left panel shows that the $M_{\text{ej}}\text{--}f_{\text{dep}}$ relation is tightly clustered for $M_{\text{ZAMS}} \leq 9.5 M_{\odot}$ but exhibits significant deviation for more massive models. Even within this narrow mass range of $1 M_{\odot}$, the ejected fraction ($M_{\text{ej}}/M_{\text{Henv}}$) can vary by a factor of ~ 10 at fixed f_{dep} . The dotted curves show power-law fits to these relations for each stellar model with the same color. For the 2 more massive models (9.75 and $10.0 M_{\odot}$), we limit the fit to $f_{\text{dep}} \leq 0.8$, as the entire H-rich envelope is ejected at a smaller value of f_{dep} (~ 0.85). The power-law index lies in the range of ~ 10.6 to 13.9 without a monotonic trend with M_{ZAMS} .

The right panel further illustrates the relation between M_{ej} and f_{gain} . The dotted and dashed curves represent the fit for the $9 M_{\odot}$ model and the fit scaled upward by a factor of 2.6, respectively. The tight clustering in this plane demonstrates the potential to constrain the energy gained by the H-rich envelope by M_{ej} during such a pre-SN eruption event.

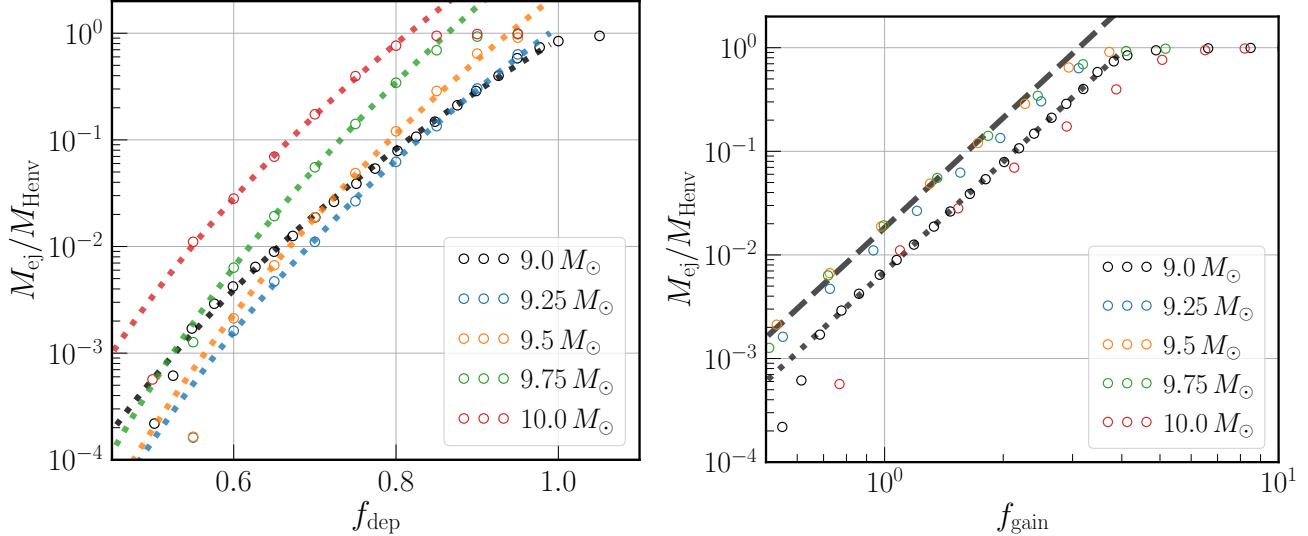


Figure 6. Same as Figure 5, but for the progenitor dependence with all data measured at 3 years post energy deposition. In the left panel, the dotted curves are power-law fits to the data with indices of ~ 10.6 - 13.9 . We fit the data over $f_{\text{dep}} = 0.55$ - 1.0 for models with $M_{\text{ZAMS}} \leq 9.5 M_{\odot}$, and over $f_{\text{dep}} = 0.55$ - 0.8 for the two more massive models. In the right panel, the black dotted curve shows the power-law fit for the $9.0 M_{\odot}$ model, and the dashed curve is the same fit scaled upward by a factor of 2.6.

3. RADIATIVE-TRANSFER SIMULATION

3.1. Methodology

A direct observational signature of the late-stage eruptions in CCSN progenitors is precursor electromagnetic transients (L. Dessart et al. 2010; D. Tsuna et al. 2023; T. Matsumoto & B. D. Metzger 2022). To model such transients, we perform radiative-transfer simulations using the multi-group radiative hydrodynamics code **STELLA** (S. I. Blinnikov et al. 1998; S. Blinnikov et al. 2000; S. I. Blinnikov et al. 2006), available in the **MESA** software suite (r21.12.1; B. Paxton et al. 2018). As a widely-used code for modeling supernova light curves, **STELLA** solves the radiative transfer equation with a two-moment scheme that employs the variable Eddington factor method (S. I. Blinnikov et al. 1998). It utilizes an EOS that includes ions, electrons, and positrons complemented with a Saha solver (S. I. Blinnikov & N. V. Dunina-Barkovskaya 1994; S. Blondin et al. 2022), and accounts opacities from photoionization, free-free absorption, electron scattering, and line interactions (R. G. Eastman & P. A. Pinto 1993; R. L. Kurucz &

B. Bell 1995; D. A. Verner & D. G. Yakovlev 1995; D. A. Verner et al. 1996). Radiation acceleration is computed using the first radiation moment (flux).

We extract the stellar structure from the eruption simulations when the shock reaches a mass coordinate of $0.2 M_{\odot}$ below the surface and use it as input for **STELLA**. The simulations preserve the original **SNEC** grid (cf. § 2.1) and employ 40 energy bins spanning 1-50000 Å for the spectral energy distribution (SED) of photons. We simulate only the $9.0 M_{\odot}$ model, as other models are expected to follow similar trends with E_{dep} .

3.2. Precursor signals

Figure 7 presents the bolometric light curves and black-body temperature (T_{bb}) evolution of the precursor emission for selected values of f_{dep} . The bolometric luminosity (L_{bol}) is integrated from the SED in the outermost zone, and T_{bb} is derived from its black-body fit. Following a brief shock breakout pulse near time zero, all models exhibit a main emission phase lasting hundreds of days. The peak luminosities in this phase range from $10^{38.5}$ to $10^{40} \text{ erg s}^{-1}$, approx-

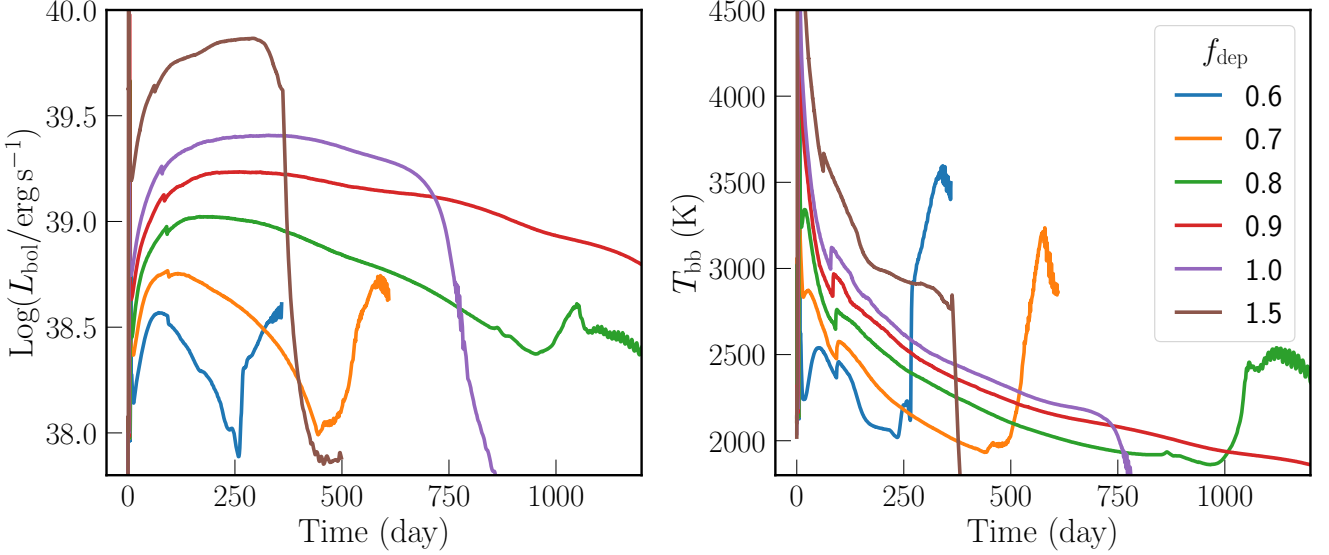


Figure 7. Bolometric light curves (left panel) and black-body temperature evolution (right panel) for the $9.0 M_{\odot}$ eruption models at selected values of f_{dep} . Time zero is defined as the beginning of STELLA simulations.

imately an order of magnitude fainter than the plateau of the observed least luminous SNe IIP (K. K. Das et al. 2025b). As expected, a larger f_{dep} produces a brighter peak. As found in L. Dessart et al. (2010), the light-curve morphology evolves systematically with f_{dep} . For small values (0.6-0.8), L_{bol} reaches the peak at ~ 100 -200 days and then decays linearly in log space to $\sim 10^{38} \text{ erg s}^{-1}$. For an intermediate value ($f_{\text{dep}} = 0.9$), the decay is significantly slower and L_{bol} maintains $\sim 10^{39} \text{ erg s}^{-1}$ for more than 1000 days. At even larger values ($f_{\text{dep}} \geq 1.0$), the light curve resembles SNe IIP but with a fainter L_{bol} and a longer plateau (~ 100 days for typical SNe IIP). The time-integrated radiation energy ranges from 10^{46} to 10^{47} erg, about 10% of the energy gained by the H-rich envelope. Throughout the main emission phase, T_{bb} is in the range of 2000 to 3000 K, cooler than the ~ 6000 K plateau of typical SNe IIP, and increases systematically with greater f_{dep} .

As the radiation is primarily powered by the cooling of the H-rich ejecta, the dependence of light curves on f_{dep} directly reflects the influence of f_{dep} on the mass ejection. For a large f_{dep} , the entire H-rich envelope is ejected and the light

curves follow the scaling laws of SNe IIP (e.g., D. V. Popov 1993). In this regime, the plateau luminosity increases and its duration decreases with higher explosion energy (represented here by E_{gain}). For a small f_{dep} , both the kinetic energy and the ejected mass are reduced. The lower ejected mass leads to a shorter photon diffusion time, producing a rapidly declining light curve. As the ejecta becomes optically thin and the bound material is revealed, the emission returns to its original RSG-like state. Lastly, the long-lasting emission for $f_{\text{dep}} = 0.9$ reflects the scenario in which a large fraction of the H-rich envelope is lost and expands over a very extended period (cf. Figure 3), sustaining the cooling emission.

The brief shock breakout emission is highlighted in Figure 8, manifesting as a peak with a duration of ~ 1 day. The peak luminosity increases with f_{dep} , reaching values comparable to the plateau luminosities of low-luminosity SNe IIP for $f_{\text{dep}} \geq 1$. During this phase, T_{bb} peaks in the range of 5000-30000 K, producing emission mainly in the optical to UV bands. Although this is brighter and resides more at short wavelengths compared to the main emission epoch,

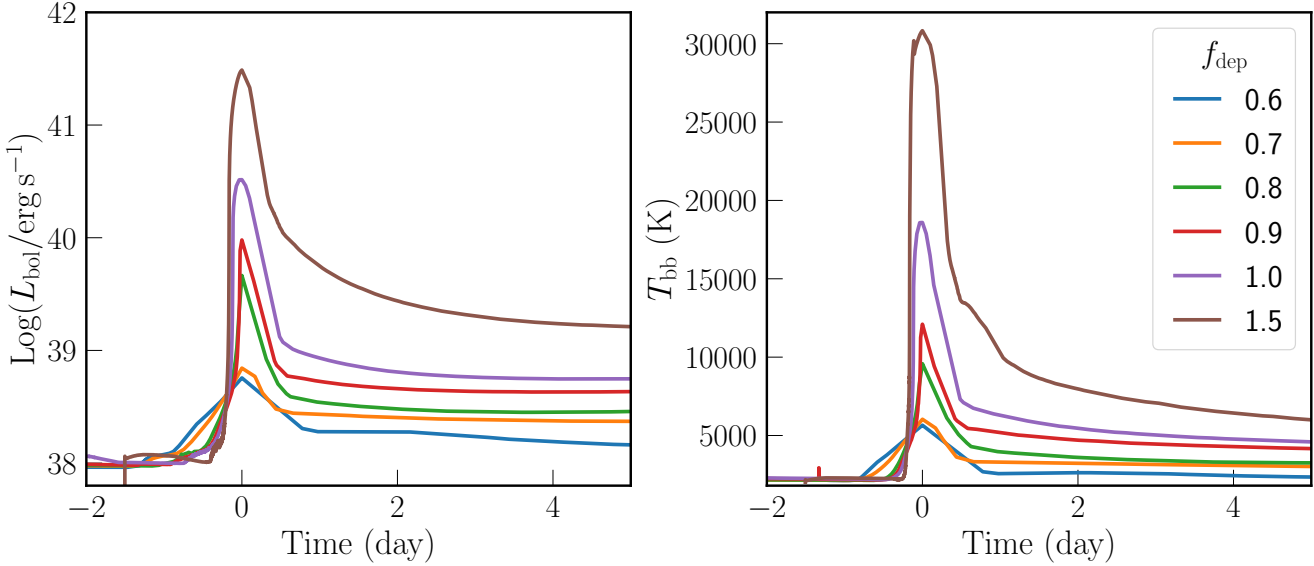


Figure 8. Bolometric light curves (left panel) and black-body temperature evolution (right panel) for the shock breakout signal of the $9.0 M_{\odot}$ eruption models at selected values of f_{dep} . Time zero is defined as the epoch of peak bolometric luminosity.

its short timescale renders it difficult to detect with current observing facilities, e.g., ZTF scans the whole northern sky every 2 nights. It can be a potential target for future high-cadence UV missions such as ULTRASAT (Y. Shvartzvald et al. 2024).

Finally, we generate multi-band photometric light curves for the stellar eruptions by convolving the SED with the filter transmissions of the Legacy Survey of Space and Time (LSST; Ž. Ivezić et al. 2019). The left panel shows a representative case of $f_{\text{dep}} = 0.8$. Due to the low T_{bb} (~ 2000 -3000 K), the absolute magnitude is higher for the more infrared bands, peaking at $M \sim -9$ for the LSST- y band. Following the peak, the magnitudes decrease approximately linearly. The right panel illustrates the dependence of the y -band light curve on f_{dep} , revealing a morphology that resembles the corresponding bolometric light curves (cf. Figure 7). Even the brightest case with $f_{\text{dep}} = 1.5$ in which the entire H-rich envelope is ejected, produces an eruption ~ 2 -3 magnitudes fainter than the SN precursors observed by ZTF ($M_r \lesssim -13$; N. L. Strotjohann et al. 2021). Therefore, either

a larger energy deposition or an additional radiation mechanism is required to account for the observed precursor luminosities. For example, increasing the deposited energy to $\sim 10^{49}$ erg ($f_{\text{dep}} \approx 5$) can produce an outburst with a magnitude of $M_r \approx -13$ and a duration of ~ 200 days.

4. DISCUSSION

Our study adopted a simplified and uniform approach by modeling the energy deposition as a single, sudden event at the base of the He layer. While this assumption is physically plausible for explosive nuclear burning, the reality may involve multiple flashes that require further dedicated stellar evolutionary modeling as S. E. Woosley & A. Heger (2015). Previous works have provided hints on the impact of varying locations, durations, and number of deposition times L. Dessart et al. (2010); D. Tsuna et al. (2023). For instance, a longer deposition duration or a deeper location can yield outcomes equivalent to a smaller net energy input. D. Tsuna et al. (2023) demonstrated that double energy depositions can produce a significant enhancement of radiation when the second ejecta

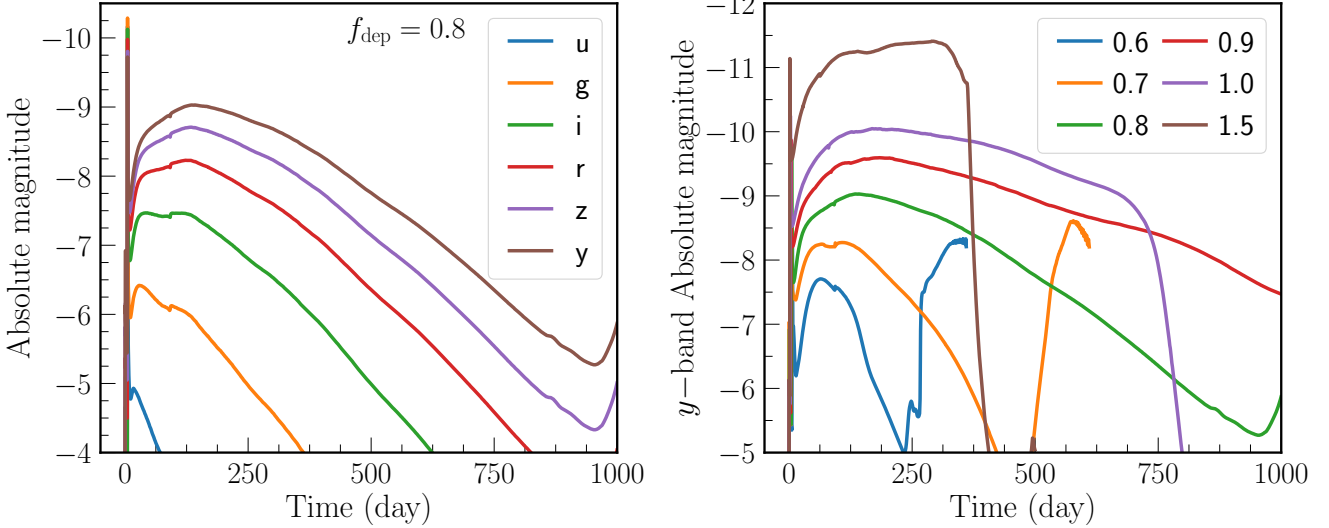


Figure 9. *Left panel:* multi-band photometric light curves with the LSST filters for the $9.0 M_{\odot}$ model at $f_{\text{dep}} = 0.8$. *Right panel:* photometric light curves in the LSST y -band for the $9.0 M_{\odot}$ model at selected values of f_{dep} .

collides with the first. Ultimately, a comprehensive understanding of these eruptions will require future models that self-consistently incorporate the detailed properties of the underlying explosive nuclear flashes.

Apart from these uncertainties, we have chosen the deposited energy to be a fraction (f_{dep}) of the total envelope binding energy $E_{\text{bind,tot}}$. As noted in § 2.1, our choice of f_{dep} in the range of 0.5-1.0 results in the mass ejection from a non-negligible fraction ($\sim 10^{-4}$) to the full envelope eruption (1.0). However, the energy released by explosive nuclear burning in the core is an intrinsic property, and it is not coupled to the envelope binding energy (S. E. Woosley & A. Heger 2015). Consequently, our exploration of the precursor light curves (cf. Figure 7) is limited to the adopted f_{dep} range and does not reflect the full possible diversity of SN precursors. We note that with $f_{\text{dep}} \approx 5$, the precursor luminosity can reach the lower limit of the observed precursor brightness by ZTF ($M_r \sim -13$; N. L. Strotjohann et al. 2021). With even larger values of f_{dep} , we expect the precursor light curve to resemble SN IIP, with its plateau luminosity

and duration following the corresponding scaling relations (D. V. Popov 1993).

Although we performed radiative-transfer simulations, their primary purpose was to generate precursor light curves. Radiative cooling also influences the mass ejection process, slowing down the outflow and modifying its temperature profile. A complete model of the CSM and progenitor appearance should further account for subsequent processes such as dust formation (P. Massey 2003; P. Massey et al. 2005; T. Verhoelst et al. 2009). To support such efforts, we provide publicly available profiles at selected epochs from both our SNEC and STELLA simulations.

Another important caveat of this study is the assumption of spherical symmetry in our hydrodynamic simulations. B. T.-H. Tsang et al. 2022 has highlighted this limitation by performing a suite of 3D pre-SN eruption simulations with a single progenitor model of $M_{\text{ZAMS}} = 15 M_{\odot}$. They demonstrated that multi-dimensional effects can lead to enhanced ejecta masses and an inhomogeneous structure in the CSM, with column densities varying by roughly an order of magnitude for different angles. However, con-

ducting such 3D simulations is prohibitive for a wide parameter space, making them unfeasible for a systematic investigation of progenitor dependence and energy deposition parameters. A potential way forward is to develop calibrated 1D prescriptions that capture the essential effects of multi-dimensional dynamics informed by 3D simulations (e.g., P. C. Duffell 2016).

5. CONCLUSIONS

In this paper, we have investigated the consequences of sudden energy deposition at the base of the He layer in low-mass CCSN progenitors of T. Sukhbold et al. (2016), a scenario that mimics the energy release from late-stage explosive nuclear flashes (T. A. Weaver & S. E. Woosley 1979; S. E. Woosley & A. Heger 2015). Using non-radiative hydrodynamics simulations with SNEC, we traced the resulting outflow to determine the final ejecta mass (defined as shells exceeding the local escaping velocity), which typically saturates within 3 years post energy deposition. We established scaling relations between the ejecta mass and both the deposited energy and the energy gained by the H-rich envelope. For the latter, we found a power-law relation with an index of ~ 3.5 , similar to studies with polytropic stars (e.g., I. Linial et al. 2021; N. J. Corso & D. Lai 2024). This relation shows limited scatter across the $9\text{-}10 M_{\odot}$ range considered, within a factor of ~ 2.6 . The shock passage flattens the bound H-rich envelope, a structural change that could affect the SN light-curve morphology and serves as an additional diagnostic for the eruption. We note that for deposited energies near the threshold of full envelope ejection, mass loss occurs over an extended period, making the determination of the final ejecta mass non-trivial.

Furthermore, we computed the associated precursor light curves for the low-mass progenitor considered ($9 M_{\odot}$), using multi-group radiative hydrodynamics simulations with STELLA. These signals are faint, with luminosities of

$\sim 10^{39} \text{ erg s}^{-1}$ sustained for hundreds of days. For low energy deposition, the light curve exhibits a linear decay after the main emission peak, with the star returning to its original RSG appearance once the ejecta becomes optically thin. In contrast, high energy deposition cases exhibit longer durations and plateau luminosities roughly an order of magnitude lower than the lowest luminosity SNe IIP (K. K. Das et al. 2025b) when the entire envelope is ejected. The precursor emission has a cool black-body temperature of $\sim 2000\text{-}3000 \text{ K}$, causing it to peak in the infrared. Although the shock breakout signal can reach SN brightness, its brevity of ~ 1 day makes it difficult to detect with current facilities. These findings are consistent with results from more massive progenitors reported in L. Dessart et al. (2010); D. Tsuna et al. (2023).

Our simulations are designed to follow the process of mass ejection and its associated radiation properties. However, the energy initially deposited is significantly consumed by the material that remains bound. The energy carried away by the ejecta and its radiated energy is a fraction of the deposited energy. For cases of weak energy deposition, only a tiny fraction is radiated promptly. For example, with $f_{\text{dep}} = 0.6$, the radiated energy is less than 10^{46} erg , compared to the deposited energy of $\sim 10^{48} \text{ erg}$. The remaining energy may be stored in the bound envelope as thermal energy and can later be radiated away as the ejecta becomes optically thin. To fully understand the impact of inner energy deposition on pre-SN emission, it is essential to model the secular evolution of the perturbed bound envelope. Considering the long timescale, this is most feasibly achieved with quasi-static radiation transfer.

DATA AVAILABILITY

The numerical results of this work, including the profiles of the evolved envelope and circumstellar material, and light curves of the erup-

tions, are publicly available at the Science Data Bank doi: [10.57760/sciedb.31295](https://doi.org/10.57760/sciedb.31295).

ACKNOWLEDGMENTS

We thank the anonymous referee for their constructive comments. We thank Dong Lai and Evan O'Connor for their stimulating conversations. This work is supported by the National Natural Science Foundation of China (NSFC, grant Nos. 12288102, 12125303, 12090040/3, 12393811, 12473031), the Strategic Priority Research Program of the Chinese Academy of Sciences (grant Nos. XDB1160301, XDB1160300, XDB1160000), the National Key R&D Program of China (grant No. 2021YFA1600401/2021YFA1600403), Yunnan Key Laboratory of Supernova Research (No. 202505AV340004), the Yunnan Revitalization Talent Support Program—Science & Technology Champion Project (No.202305AB35003),

the Yunnan Revitalization Talent Support Program—Young Talent project, and the Yunnan Fundamental Research Projects (grant Nos. 202501AS070078, 202401BC070007). The authors gratefully acknowledge the “PHOENIX Supercomputing Platform” jointly operated by the Binary Population Synthesis Group and the Stellar Astrophysics Group at Yunnan Observatories, CAS. H. L. was supported by the National Natural Science Foundation of China (NSFC grants No. 12403061) and the innovative project of ‘Caiyun Postdoctoral Project’ of Yunnan Province.

Software: SNEC (V. Morozova et al. 2015); STELLA (S. I. Blinnikov et al. 1998; S. Blinnikov et al. 2000; S. I. Blinnikov et al. 2006; B. Paxton et al. 2018); Astropy (Astropy Collaboration et al. 2022); Numpy (C. R. Harris et al. 2020); Matplotlib (J. D. Hunter 2007)

REFERENCES

Arnett, W. D., & Meakin, C. 2011, ApJ, 733, 78, doi: [10.1088/0004-637X/733/2/78](https://doi.org/10.1088/0004-637X/733/2/78)

Astropy Collaboration, Price-Whelan, A. M., Lim, P. L., et al. 2022, ApJ, 935, 167, doi: [10.3847/1538-4357/ac7c74](https://doi.org/10.3847/1538-4357/ac7c74)

Barkat, Z., Rakavy, G., & Sack, N. 1967, PhRvL, 18, 379, doi: [10.1103/PhysRevLett.18.379](https://doi.org/10.1103/PhysRevLett.18.379)

Barker, B. L., Harris, C. E., Warren, M. L., O'Connor, E. P., & Couch, S. M. 2022, ApJ, 934, 67, doi: [10.3847/1538-4357/ac77f3](https://doi.org/10.3847/1538-4357/ac77f3)

Bennett, P. D. 2010, in Astronomical Society of the Pacific Conference Series, Vol. 425, Hot and Cool: Bridging Gaps in Massive Star Evolution, ed. C. Leitherer, P. D. Bennett, P. W. Morris, & J. T. Van Loon, 181, doi: [10.48550/arXiv.1004.1853](https://doi.org/10.48550/arXiv.1004.1853)

Bilinski, C., Smith, N., Li, W., et al. 2015, MNRAS, 450, 246, doi: [10.1093/mnras/stv566](https://doi.org/10.1093/mnras/stv566)

Blinnikov, S., Lundqvist, P., Bartunov, O., Nomoto, K., & Iwamoto, K. 2000, ApJ, 532, 1132, doi: [10.1086/308588](https://doi.org/10.1086/308588)

Blinnikov, S. I., & Dunina-Barkovskaya, N. V. 1994, MNRAS, 266, 289, doi: [10.1093/mnras/266.2.289](https://doi.org/10.1093/mnras/266.2.289)

Blinnikov, S. I., Eastman, R., Bartunov, O. S., Popolitov, V. A., & Woosley, S. E. 1998, ApJ, 496, 454, doi: [10.1086/305375](https://doi.org/10.1086/305375)

Blinnikov, S. I., Röpke, F. K., Sorokina, E. I., et al. 2006, A&A, 453, 229, doi: [10.1051/0004-6361:20054594](https://doi.org/10.1051/0004-6361:20054594)

Blondin, S., Blinnikov, S., Callan, F. P., et al. 2022, A&A, 668, A163, doi: [10.1051/0004-6361/202244134](https://doi.org/10.1051/0004-6361/202244134)

Brennan, S. J., Sollerman, J., Irani, I., et al. 2024, A&A, 684, L18, doi: [10.1051/0004-6361/202449350](https://doi.org/10.1051/0004-6361/202449350)

Bruch, R. J., Gal-Yam, A., Schulze, S., et al. 2021, ApJ, 912, 46, doi: [10.3847/1538-4357/abef05](https://doi.org/10.3847/1538-4357/abef05)

Bruch, R. J., Gal-Yam, A., Yaron, O., et al. 2023, ApJ, 952, 119, doi: [10.3847/1538-4357/acd8be](https://doi.org/10.3847/1538-4357/acd8be)

Chambers, K. C., Magnier, E. A., Metcalfe, N., et al. 2016, arXiv e-prints, arXiv:1612.05560, doi: [10.48550/arXiv.1612.05560](https://doi.org/10.48550/arXiv.1612.05560)

Cheng, S. J., Goldberg, J. A., Cantiello, M., et al. 2024, *ApJ*, 974, 270, doi: [10.3847/1538-4357/ad701e](https://doi.org/10.3847/1538-4357/ad701e)

Chevalier, R. A. 2012, *ApJL*, 752, L2, doi: [10.1088/2041-8205/752/1/L2](https://doi.org/10.1088/2041-8205/752/1/L2)

Corso, N. J., & Lai, D. 2024, *ApJ*, 967, 33, doi: [10.3847/1538-4357/ad3e6c](https://doi.org/10.3847/1538-4357/ad3e6c)

Couch, S. M., Warren, M. L., & O'Connor, E. P. 2020, *ApJ*, 890, 127, doi: [10.3847/1538-4357/ab609e](https://doi.org/10.3847/1538-4357/ab609e)

Danieli, B., & Soker, N. 2019, *MNRAS*, 482, 2277, doi: [10.1093/mnras/sty2892](https://doi.org/10.1093/mnras/sty2892)

Das, K. K., Kasliwal, M. M., Fremling, C., et al. 2025a, *PASP*, 137, 044203, doi: [10.1088/1538-3873/adcaeb](https://doi.org/10.1088/1538-3873/adcaeb)

Das, K. K., Kasliwal, M. M., Sollerman, J., et al. 2025b, arXiv e-prints, arXiv:2506.20068, doi: [10.48550/arXiv.2506.20068](https://doi.org/10.48550/arXiv.2506.20068)

Davies, B., & Beasor, E. R. 2020, *MNRAS*, 493, 468, doi: [10.1093/mnras/staa174](https://doi.org/10.1093/mnras/staa174)

Davies, B., Plez, B., & Petrault, M. 2022, *MNRAS*, 517, 1483, doi: [10.1093/mnras/stac2427](https://doi.org/10.1093/mnras/stac2427)

Dessart, L., Hillier, D. J., & Audit, E. 2017, *A&A*, 605, A83, doi: [10.1051/0004-6361/201730942](https://doi.org/10.1051/0004-6361/201730942)

Dessart, L., Hillier, D. J., Waldman, R., & Livne, E. 2013, *MNRAS*, 433, 1745, doi: [10.1093/mnras/stt861](https://doi.org/10.1093/mnras/stt861)

Dessart, L., Livne, E., & Waldman, R. 2010, *MNRAS*, 405, 2113, doi: [10.1111/j.1365-2966.2010.16626.x](https://doi.org/10.1111/j.1365-2966.2010.16626.x)

Duffell, P. C. 2016, *ApJ*, 821, 76, doi: [10.3847/0004-637X/821/2/76](https://doi.org/10.3847/0004-637X/821/2/76)

Eastman, R. G., & Pinto, P. A. 1993, *ApJ*, 412, 731, doi: [10.1086/172957](https://doi.org/10.1086/172957)

Foley, R. J., Berger, E., Fox, O., et al. 2011, *ApJ*, 732, 32, doi: [10.1088/0004-637X/732/1/32](https://doi.org/10.1088/0004-637X/732/1/32)

Förster, F., Moriya, T. J., Maureira, J. C., et al. 2018, *Nature Astronomy*, 2, 808, doi: [10.1038/s41550-018-0563-4](https://doi.org/10.1038/s41550-018-0563-4)

Fuller, J. 2017, *MNRAS*, 470, 1642, doi: [10.1093/mnras/stx1314](https://doi.org/10.1093/mnras/stx1314)

Fuller, J., & Tsuna, D. 2024, *The Open Journal of Astrophysics*, 7, 47, doi: [10.33232/001c.120130](https://doi.org/10.33232/001c.120130)

Gal-Yam, A., Arcavi, I., Ofek, E. O., et al. 2014, *Nature*, 509, 471, doi: [10.1038/nature13304](https://doi.org/10.1038/nature13304)

Graham, M. J., Kulkarni, S. R., Bellm, E. C., et al. 2019, *PASP*, 131, 078001, doi: [10.1088/1538-3873/ab006c](https://doi.org/10.1088/1538-3873/ab006c)

Harris, C. R., Millman, K. J., van der Walt, S. J., et al. 2020, *Nature*, 585, 357

Hunter, J. D. 2007, *Computing in Science & Engineering*, 9, 90, doi: [10.1109/MCSE.2007.55](https://doi.org/10.1109/MCSE.2007.55)

Ibeling, D., & Heger, A. 2013, *ApJL*, 765, L43, doi: [10.1088/2041-8205/765/2/L43](https://doi.org/10.1088/2041-8205/765/2/L43)

Ivezić, Ž., Kahn, S. M., Tyson, J. A., et al. 2019, *ApJ*, 873, 111, doi: [10.3847/1538-4357/ab042c](https://doi.org/10.3847/1538-4357/ab042c)

Jacobson-Galán, W. V., Dessart, L., Jones, D. O., et al. 2022, *ApJ*, 924, 15, doi: [10.3847/1538-4357/ac3f3a](https://doi.org/10.3847/1538-4357/ac3f3a)

Jiang, Y.-F., Cantiello, M., Bildsten, L., et al. 2018, *Nature*, 561, 498, doi: [10.1038/s41586-018-0525-0](https://doi.org/10.1038/s41586-018-0525-0)

Jones, S., Hirschi, R., & Nomoto, K. 2014, *ApJ*, 797, 83, doi: [10.1088/0004-637X/797/2/83](https://doi.org/10.1088/0004-637X/797/2/83)

Jones, S., Hirschi, R., Nomoto, K., et al. 2013, *ApJ*, 772, 150, doi: [10.1088/0004-637X/772/2/150](https://doi.org/10.1088/0004-637X/772/2/150)

Khazov, D., Yaron, O., Gal-Yam, A., et al. 2016, *ApJ*, 818, 3, doi: [10.3847/0004-637X/818/1/3](https://doi.org/10.3847/0004-637X/818/1/3)

Kippenhahn, R., Weigert, A., & Weiss, A. 2013, *Stellar Structure and Evolution*, doi: [10.1007/978-3-642-30304-3](https://doi.org/10.1007/978-3-642-30304-3)

Kozyreva, A., Janka, H.-T., Kresse, D., Taubenberger, S., & Baklanov, P. 2022, *MNRAS*, 514, 4173, doi: [10.1093/mnras/stac1518](https://doi.org/10.1093/mnras/stac1518)

Kuriyama, N., & Shigeyama, T. 2020, *A&A*, 635, A127, doi: [10.1051/0004-6361/201937226](https://doi.org/10.1051/0004-6361/201937226)

Kurucz, R. L., & Bell, B. 1995, *Atomic line list*

Langer, N. 2012, *ARA&A*, 50, 107, doi: [10.1146/annurev-astro-081811-125534](https://doi.org/10.1146/annurev-astro-081811-125534)

Leonard, D. C., Filippenko, A. V., Barth, A. J., & Matheson, T. 2000, *ApJ*, 536, 239, doi: [10.1086/308910](https://doi.org/10.1086/308910)

Leung, S.-C., & Fuller, J. 2020, *ApJ*, 900, 99, doi: [10.3847/1538-4357/abac5d](https://doi.org/10.3847/1538-4357/abac5d)

Limongi, M., Roberti, L., Chieffi, A., & Nomoto, K. 2024, *ApJS*, 270, 29, doi: [10.3847/1538-4365/ad12c1](https://doi.org/10.3847/1538-4365/ad12c1)

Lin, H., Zhang, J., Wang, X., et al. 2025, *MNRAS*, 540, 2591, doi: [10.1093/mnras/staf893](https://doi.org/10.1093/mnras/staf893)

Linial, I., Fuller, J., & Sari, R. 2021, *MNRAS*, 501, 4266, doi: [10.1093/mnras/staa3969](https://doi.org/10.1093/mnras/staa3969)

Maeder, A., & Meynet, G. 1987, *A&A*, 182, 243

Massey, P. 2003, *ARA&A*, 41, 15, doi: [10.1146/annurev.astro.41.071601.170033](https://doi.org/10.1146/annurev.astro.41.071601.170033)

Massey, P., Plez, B., Levesque, E. M., et al. 2005, *ApJ*, 634, 1286, doi: [10.1086/497065](https://doi.org/10.1086/497065)

Matsumoto, T., & Metzger, B. D. 2022, *ApJ*, 936, 114, doi: [10.3847/1538-4357/ac892c](https://doi.org/10.3847/1538-4357/ac892c)

Matzner, C. D., & Ro, S. 2021, *ApJ*, 908, 23, doi: [10.3847/1538-4357/abd03b](https://doi.org/10.3847/1538-4357/abd03b)

Mauerhan, J. C., Smith, N., Filippenko, A. V., et al. 2013, *MNRAS*, 430, 1801, doi: [10.1093/mnras/stt009](https://doi.org/10.1093/mnras/stt009)

Maund, J. R., Smartt, S. J., & Danziger, I. J. 2005, *MNRAS*, 364, L33, doi: [10.1111/j.1745-3933.2005.00100.x](https://doi.org/10.1111/j.1745-3933.2005.00100.x)

Maza, J., Hamuy, M., Antezana, R., et al. 2009, Central Bureau Electronic Telegrams, 1928, 1

Moriya, T. J., Subrayan, B. M., Milisavljevic, D., & Blinnikov, S. I. 2023, *PASJ*, 75, 634, doi: [10.1093/pasj/psad024](https://doi.org/10.1093/pasj/psad024)

Moriya, T. J., Yoon, S.-C., Gräfener, G., & Blinnikov, S. I. 2017, *MNRAS*, 469, L108, doi: [10.1093/mnrasl/slx056](https://doi.org/10.1093/mnrasl/slx056)

Morozova, V., Piro, A. L., Fuller, J., & Van Dyk, S. D. 2020, *ApJL*, 891, L32, doi: [10.3847/2041-8213/ab77c8](https://doi.org/10.3847/2041-8213/ab77c8)

Morozova, V., Piro, A. L., Renzo, M., et al. 2015, *ApJ*, 814, 63, doi: [10.1088/0004-637X/814/1/63](https://doi.org/10.1088/0004-637X/814/1/63)

Nomoto, K., & Hashimoto, M.-A. 1986, *Progress in Particle and Nuclear Physics*, 17, 267, doi: [10.1016/0146-6410\(86\)90021-9](https://doi.org/10.1016/0146-6410(86)90021-9)

Ofek, E. O., Sullivan, M., Shaviv, N. J., et al. 2014, *ApJ*, 789, 104, doi: [10.1088/0004-637X/789/2/104](https://doi.org/10.1088/0004-637X/789/2/104)

Ouchi, R., & Maeda, K. 2019, *ApJ*, 877, 92, doi: [10.3847/1538-4357/ab1a37](https://doi.org/10.3847/1538-4357/ab1a37)

Ouchi, R., & Maeda, K. 2021, *MNRAS*, 500, 1889, doi: [10.1093/mnras/staa2527](https://doi.org/10.1093/mnras/staa2527)

Owocki, S. P., Hirai, R., Podsiadlowski, P., & Schneider, F. R. N. 2019, *MNRAS*, 485, 988, doi: [10.1093/mnras/stz461](https://doi.org/10.1093/mnras/stz461)

Paczynski, B. 1983, *ApJ*, 267, 315, doi: [10.1086/160870](https://doi.org/10.1086/160870)

Pastorello, A., Reguitti, A., Tartaglia, L., et al. 2025, *A&A*, 701, A32, doi: [10.1051/0004-6361/202554858](https://doi.org/10.1051/0004-6361/202554858)

Paxton, B., Schwab, J., Bauer, E. B., et al. 2018, *ApJS*, 234, 34, doi: [10.3847/1538-4365/aaa5a8](https://doi.org/10.3847/1538-4365/aaa5a8)

Popov, D. V. 1993, *ApJ*, 414, 712, doi: [10.1086/173117](https://doi.org/10.1086/173117)

Quataert, E., & Shiode, J. 2012, *MNRAS*, 423, L92, doi: [10.1111/j.1745-3933.2012.01264.x](https://doi.org/10.1111/j.1745-3933.2012.01264.x)

Salpeter, E. E. 1955, *ApJ*, 121, 161, doi: [10.1086/145971](https://doi.org/10.1086/145971)

Sato, M., Tominaga, N., Blinnikov, S. I., et al. 2024, *ApJ*, 970, 163, doi: [10.3847/1538-4357/ad50cb](https://doi.org/10.3847/1538-4357/ad50cb)

Shappee, B., Prieto, J., Stanek, K. Z., et al. 2014, in American Astronomical Society Meeting Abstracts, Vol. 223, American Astronomical Society Meeting Abstracts #223, 236.03

Shvartzvald, Y., Waxman, E., Gal-Yam, A., et al. 2024, *ApJ*, 964, 74, doi: [10.3847/1538-4357/ad2704](https://doi.org/10.3847/1538-4357/ad2704)

Smartt, S. J. 2009, *ARA&A*, 47, 63, doi: [10.1146/annurev-astro-082708-101737](https://doi.org/10.1146/annurev-astro-082708-101737)

Smartt, S. J. 2015, *PASA*, 32, e016, doi: [10.1017/pasa.2015.17](https://doi.org/10.1017/pasa.2015.17)

Smith, N. 2017, in *Handbook of Supernovae*, ed. A. W. Alsabti & P. Murdin, 403, doi: [10.1007/978-3-319-21846-5_38](https://doi.org/10.1007/978-3-319-21846-5_38)

Smith, N., & Arnett, W. D. 2014, *ApJ*, 785, 82, doi: [10.1088/0004-637X/785/2/82](https://doi.org/10.1088/0004-637X/785/2/82)

Smith, N., Mauerhan, J. C., Cenko, S. B., et al. 2015, *MNRAS*, 449, 1876, doi: [10.1093/mnras/stv354](https://doi.org/10.1093/mnras/stv354)

Soker, N. 2021, *ApJ*, 906, 1, doi: [10.3847/1538-4357/abca8f](https://doi.org/10.3847/1538-4357/abca8f)

Stockinger, G., Janka, H. T., Kresse, D., et al. 2020, *MNRAS*, 496, 2039, doi: [10.1093/mnras/staa1691](https://doi.org/10.1093/mnras/staa1691)

Strötjohann, N. L., Ofek, E. O., Gal-Yam, A., et al. 2021, *ApJ*, 907, 99, doi: [10.3847/1538-4357/abd032](https://doi.org/10.3847/1538-4357/abd032)

Sukhbold, T., Ertl, T., Woosley, S. E., Brown, J. M., & Janka, H. T. 2016, *ApJ*, 821, 38, doi: [10.3847/0004-637X/821/1/38](https://doi.org/10.3847/0004-637X/821/1/38)

Sukhbold, T., Woosley, S. E., & Heger, A. 2018, *ApJ*, 860, 93, doi: [10.3847/1538-4357/aac2da](https://doi.org/10.3847/1538-4357/aac2da)

Timmes, F. X., & Arnett, D. 1999, *ApJS*, 125, 277, doi: [10.1086/313271](https://doi.org/10.1086/313271)

Timmes, F. X., & Swesty, F. D. 2000, *ApJS*, 126, 501, doi: [10.1086/313304](https://doi.org/10.1086/313304)

Tonry, J. L., Denneau, L., Heinze, A. N., et al. 2018, *PASP*, 130, 064505, doi: [10.1088/1538-3873/aabadf](https://doi.org/10.1088/1538-3873/aabadf)

Tsang, B. T.-H., Kasen, D., & Bildsten, L. 2022, *ApJ*, 936, 28, doi: [10.3847/1538-4357/ac83bc](https://doi.org/10.3847/1538-4357/ac83bc)

Tsuna, D., Takei, Y., & Shigeyama, T. 2023, *ApJ*, 945, 104, doi: [10.3847/1538-4357/acbbc6](https://doi.org/10.3847/1538-4357/acbbc6)

Van Dyk, S. D., Davidge, T. J., Elias-Rosa, N., et al. 2012, *AJ*, 143, 19, doi: [10.1088/0004-6256/143/1/19](https://doi.org/10.1088/0004-6256/143/1/19)

Verhoelst, T., van der Zypen, N., Hony, S., et al. 2009, A&A, 498, 127, doi: [10.1051/0004-6361/20079063](https://doi.org/10.1051/0004-6361/20079063)

Verner, D. A., Verner, E. M., & Ferland, G. J. 1996, Atomic Data and Nuclear Data Tables, 64, 1, doi: [10.1006/adnd.1996.0018](https://doi.org/10.1006/adnd.1996.0018)

Verner, D. A., & Yakovlev, D. G. 1995, A&AS, 109, 125

Wang, T., & Burrows, A. 2024, ApJ, 969, 74, doi: [10.3847/1538-4357/ad5009](https://doi.org/10.3847/1538-4357/ad5009)

Wang, T., Liu, G., Cai, Z., et al. 2023, Science China Physics, Mechanics, and Astronomy, 66, 109512, doi: [10.1007/s11433-023-2197-5](https://doi.org/10.1007/s11433-023-2197-5)

Weaver, T. A., & Woosley, S. E. 1979, in Bulletin of the American Astronomical Society, Vol. 11, 724

Woosley, S. E., Blinnikov, S., & Heger, A. 2007, Nature, 450, 390, doi: [10.1038/nature06333](https://doi.org/10.1038/nature06333)

Woosley, S. E., & Heger, A. 2015, ApJ, 810, 34, doi: [10.1088/0004-637X/810/1/34](https://doi.org/10.1088/0004-637X/810/1/34)

Woosley, S. E., Heger, A., & Weaver, T. A. 2002, Reviews of Modern Physics, 74, 1015, doi: [10.1103/RevModPhys.74.1015](https://doi.org/10.1103/RevModPhys.74.1015)

Woosley, S. E., Weaver, T. A., & Taam, R. E. 1980, in Texas Workshop on Type I Supernovae, ed. J. C. Wheeler, 96–112

Yaron, O., Perley, D. A., Gal-Yam, A., et al. 2017, Nature Physics, 13, 510, doi: [10.1038/nphys4025](https://doi.org/10.1038/nphys4025)

Yuan, X., Li, Z., Liu, X., et al. 2020, in Society of Photo-Optical Instrumentation Engineers (SPIE) Conference Series, Vol. 11445, Ground-based and Airborne Telescopes VIII, ed. H. K. Marshall, J. Spyromilio, & T. Usuda, 114457M, doi: [10.1117/12.2562334](https://doi.org/10.1117/12.2562334)

Zaghloul, M. R., Bourham, M. A., & Doster, J. M. 2000, Journal of Physics D Applied Physics, 33, 977, doi: [10.1088/0022-3727/33/8/314](https://doi.org/10.1088/0022-3727/33/8/314)

Zha, S., Müller, B., Weir, A., & Heger, A. 2023, ApJ, 952, 155, doi: [10.3847/1538-4357/acd845](https://doi.org/10.3847/1538-4357/acd845)